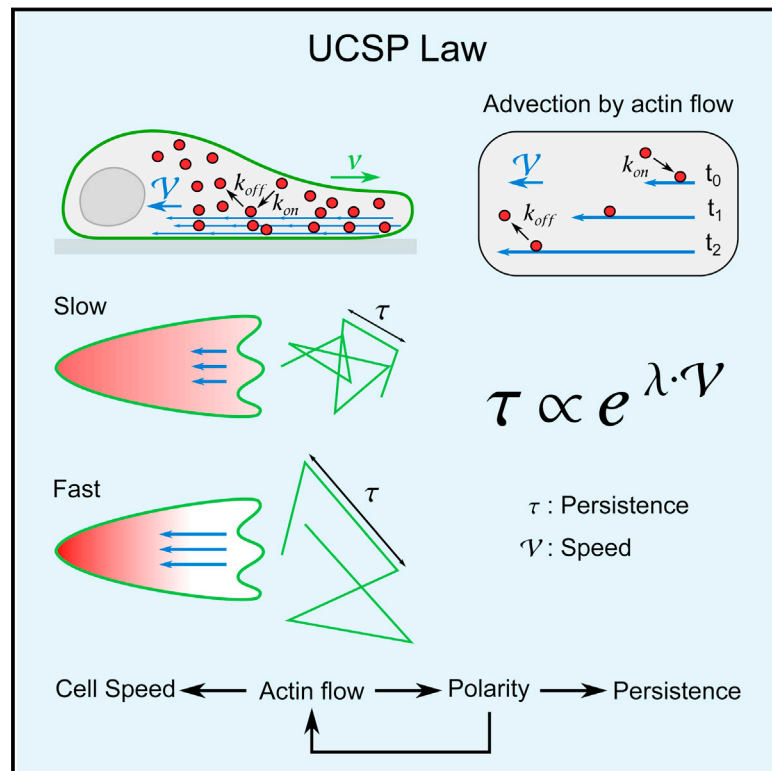


Actin Flows Mediate a Universal Coupling between Cell Speed and Cell Persistence

Graphical Abstract



Authors

Paolo Maiuri,
Jean-François Rupprecht, ...,
Michael Sixt, Raphaël Voituriez

Correspondence

matthieu.piel@curie.fr (M.P.),
sixt@ist.ac.at (M.S.),
voiturie@lptmc.jussieu.fr (R.V.)

In Brief

Despite the fact that different cell types follow distinct migration patterns, the locomotion of all cellular types follows one simple universal rule: the straightness of movement (persistence) is an exponential function of speed. This general law of cell migration is explained by a physical model based on the transport of polarity factors by the actin retrograde flows and predicts a diagram of possible cell trajectories.

Highlights

- Speed and persistence of cells are exponentially correlated (the UCSP law)
- Faster cells turn less: speed stabilizes cell directionality
- The UCSP originates from transport of polarity factors by the retrograde actin flow
- A physical model explains the UCSP and predicts a diagram of cell trajectories



Actin Flows Mediate a Universal Coupling between Cell Speed and Cell Persistence

Paolo Maiuri,^{1,9} Jean-François Rupprecht,^{2,9} Stefan Wieser,^{3,9} Verena Rupprecht,³ Olivier Bénichou,² Nicolas Carpi,¹ Mathieu Coppey,⁴ Simon De Beco,⁴ Nir Gov,⁵ Carl-Philipp Heisenberg,³ Carolina Lage Crespo,⁶ Franziska Lautenschlaeger,¹ Maël Le Berre,¹ Ana-Maria Lennon-Dumenil,⁷ Matthew Raab,¹ Hawa-Racine Thiam,¹ Matthieu Piel,^{1,*} Michael Sixt,^{3,*} and Raphaël Voituriez^{2,8,*}

¹Institut Curie, CNRS UMR 144, 26 rue d'Ulm, 75005 Paris, France

²Laboratoire de Physique Théorique de la Matière Condensée, UMR 7600 CNRS /UPMC, 4 Place Jussieu, 75255 Paris Cedex, France

³Institute of Science and Technology Austria, Am Campus 1, 3400 Klosterneuburg, Austria

⁴Institut Curie, CNRS UMR 168, 26 rue d'Ulm, 75005 Paris, France

⁵Department of Chemical Physics, Weizmann Institute of Science, 76100 Rehovot, Israel

⁶Division of Immunology, Transplantation and Infectious Diseases, San Raffaele Scientific Institute, 20132 Milan, Italy

⁷U 653, Inserm/Institut Curie, 26 rue d'Ulm, 75248 Paris Cedex 05, France

⁸Laboratoire Jean Perrin, UMR 8237 CNRS /UPMC, 4 Place Jussieu, 75255 Paris Cedex, France

⁹Co-first author

*Correspondence: matthieu.piel@curie.fr (M.P.), sixt@ist.ac.at (M.S.), voiturie@lptmc.jussieu.fr (R.V.)

<http://dx.doi.org/10.1016/j.cell.2015.01.056>

SUMMARY

Cell movement has essential functions in development, immunity, and cancer. Various cell migration patterns have been reported, but no general rule has emerged so far. Here, we show on the basis of experimental data *in vitro* and *in vivo* that cell persistence, which quantifies the straightness of trajectories, is robustly coupled to cell migration speed. We suggest that this universal coupling constitutes a generic law of cell migration, which originates in the advection of polarity cues by an actin cytoskeleton undergoing flows at the cellular scale. Our analysis relies on a theoretical model that we validate by measuring the persistence of cells upon modulation of actin flow speeds and upon optogenetic manipulation of the binding of an actin regulator to actin filaments. Beyond the quantitative prediction of the coupling, the model yields a generic phase diagram of cellular trajectories, which recapitulates the full range of observed migration patterns.

INTRODUCTION

Eukaryotic cell migration is essential for a large set of biological processes. Assessing quantitatively the exploratory efficiency of cell trajectories is therefore crucial. In the absence of external guidance, cell movement can be described as a random motion, and proposed models have ranged from simple Brownian motion to persistent random walks (Selmecki et al., 2008), Levy walks (Harris et al., 2012), or composite processes such as intermittent random walks (Bénichou et al., 2011). Such models differ in the cell persistence, which quantifies the ability of a cell to maintain its direction of motion. The variety of behaviors, observed even along a single cell trajectory, stems from the

fact that, as opposed to a passive tracer in a medium at thermal equilibrium, which performs a classical Brownian motion, a cell is self-propelled, and as such, belongs to the class of active Brownian particles (Romanczuk et al., 2012). This class of processes is extremely vast and needs to be restricted to have some predicting power. Up to now universal behaviors have emerged in the context of the collective dynamics of self-propelled particles (Czirók et al., 1998; Toner et al., 2005; Vedel et al., 2013), but remain elusive at the level of single cells.

Recently, a vast amount of data of individual cell trajectories has been collected over many cell types in the context of the First World Cell Race (Maiuri et al., 2012) (Figures 1A and 1B). These data show that, despite an apparent diversity at the level of the whole population analyzed, correlations between the mean linear instantaneous cell speed and the persistence time, defined as the mean time during which a cell maintains its direction of motion, exist. This general trend that faster cells migrate more straight than slower cells, which has since been observed by others (Wu et al., 2014), remains unexplained and suggests that robust mechanisms could constrain the possible characteristics of cell trajectories.

In this work, we analyzed trajectories of cells migrating in various *in vitro* assays and in live tissues. We reveal on the basis of this extensive data set a universal coupling between cell speed and cell persistence (UCSP). To explain what appears as a universal law of cell migration, we developed a physical model relying on minimal hypothesis that shows that actin flows, which are the hallmark of motile cells (Theriot and Mitchison, 1991; Svitkina et al., 1997; Wilson et al., 2010), reinforce cell polarity and consequently cell persistence. The model was validated experimentally by two assays: one enabling a gradual modulation of actin flow speeds combined with pharmacological interference experiments, and a second, based on an engineered optogenetic molecular module, which allowed controlling an actin polymerization regulator, Arpin. Finally, the model has the following merits: it (1) quantitatively predicts the observed exponential correlation between speed and

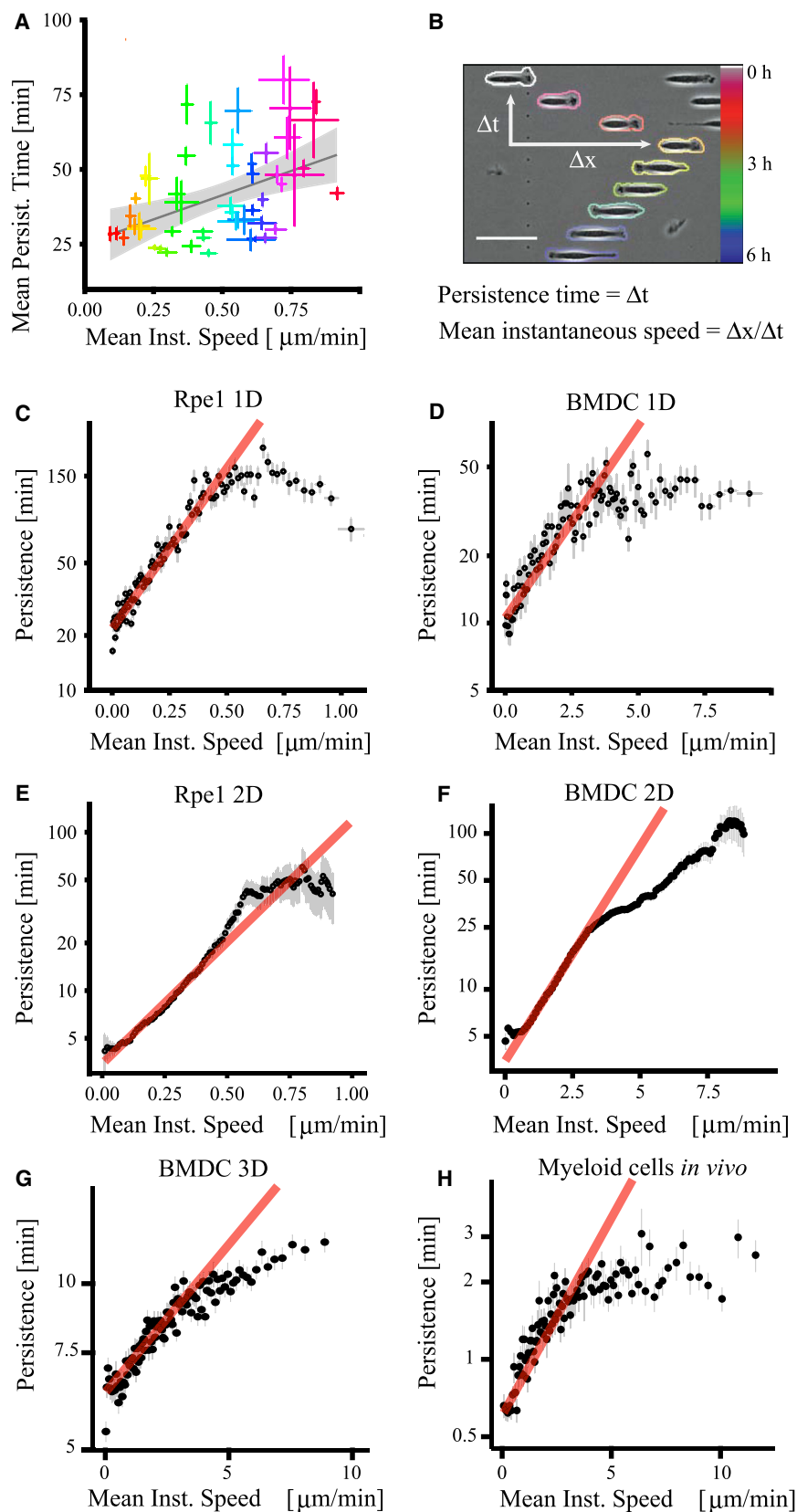


Figure 1. Correlation between Cell Persistence and Cell Speed

(A) Population mean persistence time versus mean instantaneous speed. Data from the First World Cell Race, refers to the original article (Maiuri et al., 2012) for the cell-type color code. Linear fit (solid line) and 0.95 confidence interval (gray).

(B) Definition of mean persistence time and mean instantaneous speed in 1D. Cell contour color shows the time progression. Scale bar, 50 μm .

(C–F) Persistence time, binned for the corresponding instantaneous speed, versus instantaneous speed. (C) RPE1 cells on micropatterned lines of 9- μm width coated with fibronectin. (D) BMDCs in fibronectin-treated channels with a $7 \times 5 \mu\text{m}^2$ square section. (E–F) The persistence time in 2D is defined here as the time needed for a cell to change its original direction of motion by 90° . (E) Data of RPE1 cells on 2D surface uniformly treated with fibronectin. (F) BMDCs confined between two parallel, fibronectin-treated planes, 5 μm apart from each other.

(G) BMDCs embedded in bovine collagen gel and confined between two planes 5 μm apart from each other.

(H) Myeloid cells imaged in live Medaka fish.

Red curves represent the exponential fit of the experimental data. Black dots and gray lines are mean and SE for the binned data on both axis.

See also Figures S1 and S2 and Movie S1.

persistence that characterizes the UCSP, (2) provides from minimal microscopic hypothesis an explicit construction of single cells dynamics as active Brownian particles, and (3) yields a generic phase diagram of cellular trajectories, which recapitulates the full range of observed migration behaviors.

RESULTS

Cell Trajectory Analysis Reveals a Universal Coupling between Cell Speed and Persistence

The First World Cell Race (Maiuri et al., 2012), which gathered recordings of individual cell trajectories on 1D adhesive tracks for 54 different adherent cell types made available an unprecedented amount of data. We performed a further analysis of this data and confirmed a clear positive correlation between the population averaged mean linear instantaneous cell speed and the population averaged persistence time at the level of all cell types (Figure 1A), despite their variety. To assess the robustness of this observation and check its validity at the level of single cell trajectories, we performed new experiments on two representative examples of migrating cell with either a mesenchymal migration mode (hTERT-immortalized retinal pigment epithelial cell line [RPE1]) or an amoeboid migration mode (immature bone marrow-derived mice dendritic cells [BMDC]), in various geometries (Figures S1 and S2; Movie S1): 1D adhesive tracks (Figure 1C), 1D microchannels (Figure 1D), 2D non-confined adhesive substrates (Figure 1E) and 2D confined substrates (Figure 1F). Very long cell trajectories were recorded (see Supplemental Information), allowing a clear assessment of individual cell persistence. In all cases, for which cell concentrations were low enough to treat cell trajectories as independent, we found a striking correlation between persistence time τ and mean instantaneous velocity v , which is well fitted by a simple exponential curve $\tau = Ae^{2v}$ before eventually saturating at larger v (see Discussion). We then checked whether this correlation was still valid when cells were migrating in more complex environments. We recorded BMDCs migrating in 3D collagen gels (Figure 1G) and myeloid cells migrating in live Medaka fish (Grabher et al., 2007) (Figure 1H). In both cases, persistence and speed were still highly correlated. Overall, these results show that the UCSP is robust when tested in different migration environments and organisms, and that the correlation, observed at the population level or at the level of individual cells exists all along a cell trajectory: a faster displacement is correlated with a straighter path. The analysis of this remarkably robust correlation that defines the UCSP is at the core of this work.

Faster Actin Retrograde Flow Lengthens Cell Persistence Time

To elucidate the origin of the UCSP, we reasoned that, as this law applies to all cell types we tested, including cells with very different modes of migration (mesenchymal and amoeboid cells), it had to rely on a very conserved aspect of cell locomotion. Even if many details might vary from one cell type to the other, the most conserved aspect of cell locomotion is the retrograde translocation of actin filaments in the frame of reference of the cell, from the front to the rear of its locomotory parts. Actin flows can either exist over large portions of the cell (in particular

in amoeboid cells) (Renkawitz et al., 2009), or in some cases be essentially limited to the protrusive parts (such as lamellipodia in mesenchymal cells) (Theriot and Mitchison, 1991; Svitkina et al., 1997; Wilson et al., 2010). This retrograde movement is powered by the combined forces of actin polymerization at the leading edge and actomyosin contraction at the trailing edge and represents the driving force for locomotion. Upon coupling to the environment either via transmembrane adhesion receptors of the integrin family or via friction, retrograde actin flow is turned into traction forces, which pull the cell forward while actin filaments slide to the back of the cell (Mogilner and Oster, 1996; Jurado et al., 2005; Hawkins et al., 2011).

To test if actin flows are involved in the coupling between cell persistence and cell speed, we used mature bone marrow dendritic cells (mBMDCs), for which it was already demonstrated that actin retrograde flow can be varied without affecting cell speed when substrate adhesion strength is modulated (Renkawitz et al., 2009). Indeed, the cell speed v and the velocity of the actin flow V (defined hereafter in the frame of reference of the moving cell) are usually linearly coupled according to $v = \alpha V$ (Jurado et al., 2005), such linear approximation being valid at least in the lower range of velocities for each cell type. The coefficient α models the effective friction between actin filaments and the substrate, usually mediated by specific adhesion proteins (Mitchison and Kirschner, 1988; Gardel et al., 2010) and therefore depends on experimental conditions. In some cell types, varying the actin/substrate coupling parameterized by α induces an adaptive response, which allows a cell to keep the speed of locomotion v relatively constant, despite different retrograde velocities V of the loosely coupled actin network. Such adaptation has been extensively characterized in mBMDCs. When placed in confined environments, these cells can flexibly shift between integrin-independent and integrin-dependent force transduction as even in the absence of these adhesion receptors the cells are able to generate sufficient traction to migrate. However, depletion of integrins or their ligands and the associated drop in friction causes retrograde actin slippage, which is then compensated by up to 2-fold increase in actin polymerization speed (Renkawitz et al., 2009). This property of mBMDCs moving in confined environments allowed us to independently study the influence of retrograde actin flow and actual cell speed on migratory persistence. Surface adhesion was independently controlled by depletion of $\beta 2$ integrins and their ligands (coating the surfaces with an inert PEG layer), while cell speed was gradually varied by temperature changes and by pharmacological inhibition of actomyosin contractility (blebbistatin). This allowed us to tune retrograde flows from 3 to 15 $\mu\text{m}/\text{min}$ independently of cell speed (Figure 2A). Strikingly, we observed that the mean persistence time τ measured for each experimental condition was strongly correlated with the mean speed V of the actin retrograde flow and was well-fitted by a simple exponential $\tau = A'e^{2V}$ (Figure 2B; Movie S2), whereas no correlation between τ and cell speed v was observed. Note, however, that within each experimental condition (α fixed) the linear scaling between v and V still held, so that the correlation between cell speed and cell persistence was preserved at the level of each experimental condition. These data strongly suggest that the observed UCSP originates from a coupling between cell persistence and the actin flow.

Faster Actin Retrograde Flow Enhances the Asymmetry of Polarity Cues and Stabilizes Cell Polarity

A simple hypothesis to explain these effects of actin flows would be that, in polarized migrating cells, actin flows reinforce cell polarity by enhancing the asymmetry of polarity cues, as was proposed for the establishment of polarity in early *Caenorhabditis elegans* embryos (Munro et al., 2004; Goehring et al., 2011) (Figures 2C and 2D). Examples of such cues, which are likely to vary with cell type, could be molecules responsible for the generation of contractile stress, such as myosin motors or their activators, actin polymerization regulators, or could alternatively be involved in the regulation of microtubule dynamics (Zhang et al., 2014). We introduce a first element of physical modeling to test this hypothesis. We consider a migrating cell and denote by x the coordinate in the reference frame of the moving cell, defined by the instantaneous direction of migration and by L the cell extension along this axis (Figure 2C). We are interested in the dynamics of the concentration of a generic polarity cue $c(x, t)$, which we assume here depends only on x . This cue is assumed to specify the rear part of the cell, so that $c(x=0, t) > c(x=L, t)$ for a cell moving in the + direction. The polarity cue can either diffuse in the cytosol, with diffusion coefficient D , or, depending on its affinity for actin, be advected by the cytoskeletal flow, whose velocity along x is denoted by $-V$ (with $V > 0$) in the cell reference frame. We denote by k_{on} and k_{off} the corresponding binding and unbinding rates of the cue to the actin cytoskeleton. In the limit of fast exchange (k_{on}, k_{off} large), the dynamics of $c(x, t)$ depends on advective transport and on diffusion as follows:

$$\partial_t c(x, t) - \partial_x [\tilde{V}c(x, t)] = \tilde{D}\partial_x^2 c(x, t) + \partial_x \zeta_c, \quad (\text{Equation 1})$$

where $\tilde{V} = Vk_{on}/(k_{on} + k_{off})$ and $\tilde{D} = Dk_{off}/(k_{on} + k_{off})$; here ζ_c is a Gaussian white noise that encompasses the fluctuations of the flux of cue molecules. At steady state, assuming V constant and the conservation of the total amount of cues, the mean cue concentration profile is therefore given by:

$$\bar{c}_v(x) = Ce^{-\tilde{V}x/\tilde{D}}, \quad (\text{Equation 2})$$

where C is a normalization constant and the dependence on the retrograde flow is denoted in subscript. This simple argument, which does not take into account heterogeneities in actin flows predicts simple exponential concentration profiles, whose steepness is controlled by the speed of the effective retrograde flow \tilde{V} (Figure 2D). Non-uniform actin flow profiles, as observed for example in (Wilson et al., 2010; Ofer et al., 2011) would change the exponential shape of concentration profiles, but would leave the dependence on the actin flow speed qualitatively unchanged. To check this general prediction, we measured on motile mBMDCs the concentration profiles along the polarity axis for various molecules with different affinity for actin (Figure 2E; Movie S3): Tamra (that unspecifically labels cytoplasmic proteins), Lifeact-GFP (low affinity) (Riedl et al., 2008), MLC-GFP (high affinity) (Kondo et al., 2011), and Utrophin-GFP (high affinity) (Burkel et al., 2007). As expected from the model, we observed that increasing the actin retrograde

flow could significantly increase the slope of the concentration profile of strong actin binders (MLC, Utrophin), whereas the profiles of molecules with low (Lifeact) or no (Tamra) affinity to actin remained unchanged (Figures 2E and 2F). This validates our hypothesis that actin flows reinforce the asymmetry of concentration profiles of actin binding molecules.

We next reasoned that such mechanism in principle applies to any diffusing molecule that interacts with actin, and in particular, to polarity cues. It is then expected that increasing actin flows should increase the asymmetry of the concentration profile of any polarity cue, thereby stabilizing cell polarization and consequently increasing cell persistence, according to a mechanism discussed in Svitkina et al. (1997) (note that the connection to persistence was, however, absent in this reference). To further support this hypothesis, we measured the number of protrusions for each cell, using the same nine experimental conditions to vary the actin flow and found that in conditions in which cells had a faster actin flow, there was a larger proportion of cells with a single well-polarized lamellipodium (Figures 3A, 3B, and S3). We then measured the life time of such unipolar configurations, that we call polarization time τ_p , and the actin retrograde flow speed in each protrusion, and found that they showed the same exponential correlation (Figure 3C). This suggests that the observed coupling between actin retrograde flow and cell persistence originates from the stabilization of polarity by faster actin flows, by favoring a unipolar configuration of the cell and by lengthening the protrusion lifetime.

While in principle this mechanism can apply to any diffusing polarity cue that interacts with actin, species involved in the regulation of actin flow are the most susceptible to mediate the UCSP. Cdc42, a member of the Rho GTPase family is a central regulator of polarity, mediating its function via the actin and microtubule cytoskeleton (Heasman and Ridley, 2008), and thus appeared as a natural candidate. Loss of Cdc42 in dendritic cells severely affects cell polarization and migration efficiency in vitro and in vivo (Lämmermann et al., 2009). To test if the Cdc42 polarity module was involved in coupling rearward cortical flows to polarity we selectively inhibited Cdc42 using ML-141 (Hong et al., 2013) and measured the lifetime of cell polarization τ_p in dependence of cortical flow speed V that was modulated via a set of five independent experimental conditions as discussed above (Figure 2A). As expected, inhibition of Cdc42 led to an overall reduction of the polarization lifetime for all conditions but, importantly, longer polarization lifetimes were observed for increasing actin flow speeds V and the UCSP was preserved (Figure 3D). These results indicate that the UCSP can function independently of a Cdc42-mediated signaling pathway.

We next sought to unravel key molecular polarity cues closely affected by the cortical network flow. Myosin-II is a prominent candidate, which strongly binds to actin; it is thus transported with actin flows and tends to accumulate at the cell back when actin flows are strong (Poincloux et al., 2011; Hawkins et al., 2011). It has previously been implicated in actomyosin network organization, polarized cortical architecture and migration efficiency (Vicente-Manzanares et al., 2009). Indeed, we observed that myosin II light chain localization was strongly influenced by cortical flow modulations with a more rearward accumulation

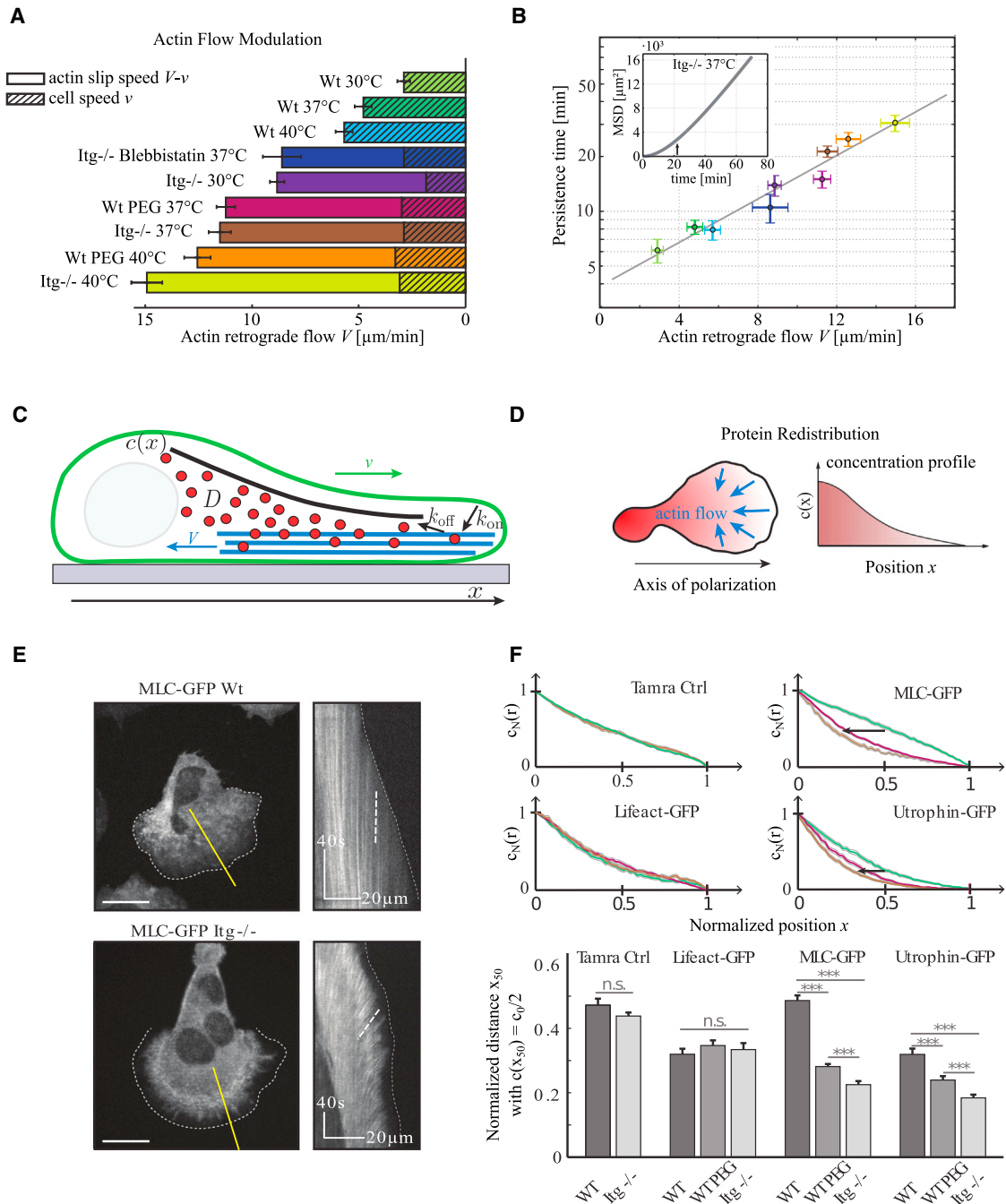


Figure 2. Modulation of Actin Retrograde Flow Speed Reveals a Positive Feedback Loop on the Stability of Cell Polarity

(A) Retrograde flow speed V in the reference frame of the cell in nine different conditions. Bars represent SEM.

(B) Cell persistence time versus retrograde flow speed. Bars represent SEM, and the gray line represents the exponential fit. Inset shows mean-square displacement plot for Itg^{-/-} cells at 37°C. Arrow highlights the crossover from persistent to random motility on longer time scales.

(C) Schematic illustrating the model with a minimal set of kinetic parameters. Polarity factors are shown as red dots, actin filaments are in blue while cell outline is green and migration substrate is gray.

(D) Schematic showing the principle of protein redistribution by the actin retrograde flow. Density of transported protein is shown in red, and depends on the position x along the cell polarity axis.

(E) Left: fluorescence images of MLC-GFP localization in migrating wild-type (Wt) and $\beta 2$ integrin knockout (Itg^{-/-}) dendritic cells under 2D confinement. Note the enhanced depletion of MLC from the leading edge in the Itg^{-/-} cell. Dashed lines indicate cell borders. Scale bar in μm . Right: kymograph performed along yellow lines. White dashed lines indicate retrograde myosin flow in the lab reference frame.

(legend continued on next page)

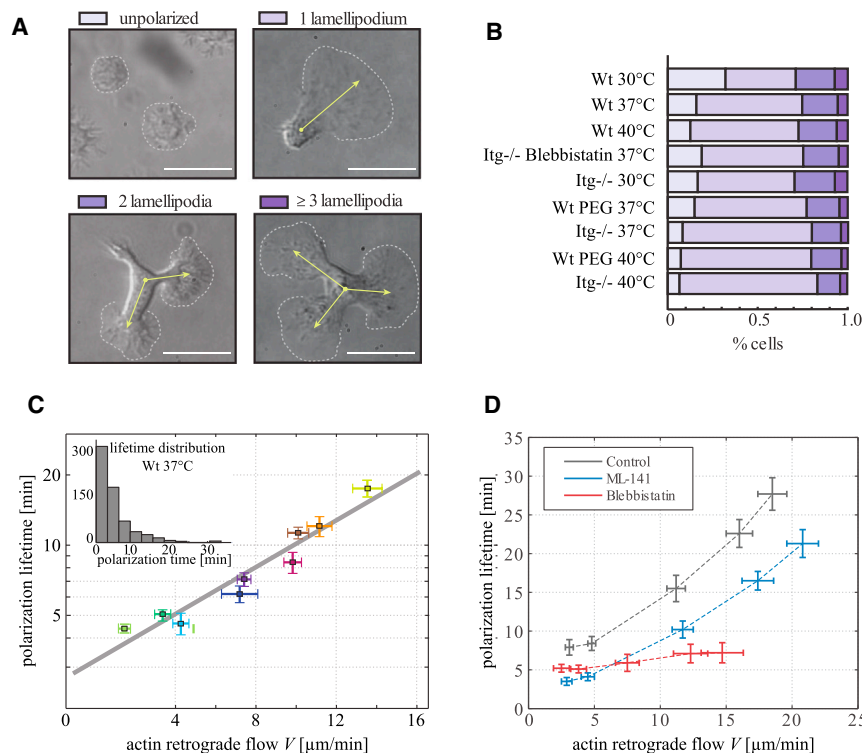


Figure 3. Stability of Cell Polarity as a Function of Actin Flow Speed and Effect of Pharmacological Inhibition of Myosin II and Cdc42 in mBMDCs

(A) Differential interference contrast (DIC) representative images of cells in the unpolarized states (no lamellipodium), polarized state (one lamellipodium), and with two lamellipodia (bi-polar) and three or more lamellipodia (multi-polar). Arrows denote the axis of polarization. Scale bar, 20 μm .

(B) Histogram of observed cell morphologies (color code see A) for nine different conditions (see Figure 2).

(C) Polarization lifetime as a function of actin flow speed. Gray line indicates exponential fits to the data. Inset shows the exponential distribution of polarization lifetimes for Wt dendritic cells at 37°C. Bars represent SEM.

(D) Polarization lifetime for control conditions (dark gray), ML-141-treated cells (Cdc42 inhibitor, blue), and Blebbistatin-treated cells (Myosin II inhibitor, red). Actin retrograde flow speed V is modulated (from left to right) using wild-type (Wt) dendritic cells (DCs) at 30°C, Wt DCs at 37°C, $\beta 2$ integrin knock-out (Itg^{-/-}) DCs at 30°C, Itg^{-/-} DCs at 40°C, and Itg^{-/-} DCs at 41.5°C. Bars represent SEM. See also Figure S3 and Movies S2 and S3.

for higher actin flow speeds V (Figure 2F). To test a potential role of myosin-II in the UCSP we pharmacologically interfered with its activity by using the myosin-II inhibitor Blebbistatin. Inhibition of Myosin-II induced a reduction of cell polarization lifetimes for all conditions and polarization lifetimes τ_p were no longer correlated to cortical flow speed V but remained at constantly low values for all V (Figure 3D). These data suggest that myosin-II constitutes an indispensable polarity cue in mBMDCs that is involved in the establishment of the UCSP.

Physical Modeling Predicts the UCSP

To substantiate our hypothesis that the UCSP originates from the coupled dynamics of actin flow and diffusing polarity cues, we developed a minimal theoretical model, which assumes that the actin flow V is also subject to fluctuations, due for example to the stochasticity of polymerization/depolymerization processes or the heterogeneity of the environment. The model, whose main ingredients are summarized below (see Supplemental Information for details), relies on the key assumption that the mean value V^* of the actin flow (for a fixed cue concentration profile) is governed by the asymmetry of the cue concentration profile. More precisely, we assume that

$$V^* = \beta(c^*(0, t) - c^*(L, t)), \quad (\text{Equation 3})$$

where β is an effective parameter that controls the intensity of the coupling between the actin flow and the asymmetry of the cue concentration profile and can be interpreted as the maximal possible velocity of the actin flow. Here, $c^*(x, t)$ denotes the fraction of activated cues, i.e., cues that induce actin flow. We show in the Supplemental Information that the phenomenological coupling (Equation 3) covers the cases where actin flows are generated by asymmetric distributions of either actin polymerization regulators (such as Arpin, see the discussion below) (Julicher et al., 2007) or activators of contractility (such as Myosin II or a Myosin II activator, as discussed above) (Hawkins et al., 2011; Bois et al., 2011; Callan-Jones and Voituriez, 2013), which are the two main scenarios that we propose. We here do not aim at describing in details the biochemical steps involved in the process and assume a classical Hill response function of index n (results are qualitatively unchanged for other choices):

$$c^*(x, t) = \frac{c^n(x, t)}{C_s^n + c^n(x, t)}. \quad (\text{Equation 4})$$

Here, C_s is the concentration of cues above which activation is saturated and is therefore determined by the maximal concentration of activated cues.

(F) Normalized concentration profiles as a function of the normalized position x along the cell polarity axis (cell front is set at $x=1$) for a set of actin-binding molecules with various actin affinity. Concentration profiles are color coded for different cell-substrate adhesion strengths (green, Wt; magenta, Wt on Peg; brown, Itg^{-/-}, all 37°C). Arrows indicate a shift of the polarity cue concentration profile toward the cell rear with increasing actin retrograde flow. (right) Normalized distance x_{50} at which the concentration drops to $c_{50} = c_0/2$ (***) $p < 0.001$, n.s. not significant.

See also Movies S2 and S3.

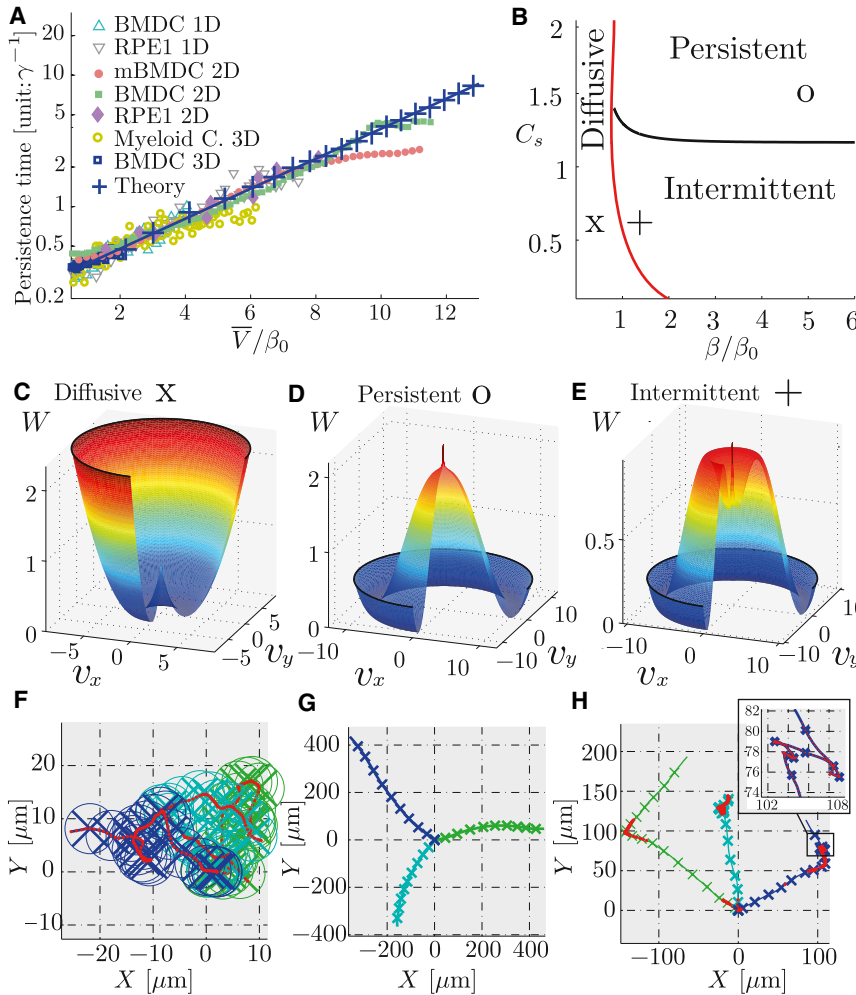


Figure 4. Model Predictions: The UCSP Law and Phase Diagram of Cell Trajectories

The values of the parameters used in the figure (except for β, C_s) and the fitting procedure are described in the [Supplemental Information](#).

(A) Persistence time as a function of the normalized mean velocity \bar{V}/β_0 , where $\beta_0 \equiv \bar{D}/L$ for the prediction of the model and for all available experimental data (rescaled).

(B) Phase diagram of cell trajectories in the β (maximal actin flow speed) and C_s (maximal concentration of activated cues) plane. Symbols correspond to the parameters used in (C) and (F) (x), (D) and (G) (0), and (E) and (H) (+).

(C–E) Effective potential W as a function of the velocities V_x and V_y normalized by β_0 . The singularity in W at the origin $V = 0$ is due to the anisotropy of the diffusion process ([Romanczuk et al., 2012](#)). (C) W is locally quadratic for V small: diffusive phase (marked by x in B). (D) W has a “sombbrero” shape: persistent phase (marked by 0 in B). (E) W has a mixed shape: intermittent phase (marked by + in B).

(F–H) Examples of simulated trajectories in the diffusive (F), persistent (G), and intermittent phases (H). Colored crosses indicate the positions at regular time intervals. Circles in (F) indicate the cell size L .

See also [Figures S4 and S5](#).

and K controls their amplitude, the effective force $\mathcal{F}(V)$ and noise intensity $\sigma(V)$ are given explicitly in the [Supplemental Information](#). The dynamics of V , fully defined by Equation 5, is therefore the dynamics of a Brownian particle in a force field $\mathcal{F}(V)$ in the presence of a non-trivial noise with additive and multiplicative

Next, we make use of the fact that the typical diffusion time of cues over the cell length L^2/D (of the order of seconds) is significantly shorter than the characteristic timescale of fluctuations in the actin flow γ^{-1} (of the order of minutes). The concentration of cues is then taken at steady state, and Equation 1 implies that it is a Poisson random variable, i.e., $c(x, t) = \bar{c}_V(x) + \delta c$ with $\overline{\delta c^2} = K_c \bar{c}_V(x)$, where K_c is a constant that controls the intensity of the particle number fluctuations and $\bar{c}_V(x)$ is the steady-state profile defined in Equation 2. Considering a cell moving on a 2D substrate (the 1D case is then deduced by taking a vanishing angular diffusion, and the generalization to 3D migration is straightforward, see [Supplemental Information](#)), the dynamics of the actin flow velocity \mathbf{V} , which is a vector of modulus V and polar angle ϕ , can then be written after linearization with respect to δc (see [Supplemental Information](#) for details):

$$\begin{aligned} \partial_t V &= \gamma \mathcal{F}(V) + \sigma(V) \zeta_V \\ \partial_t \phi &= \frac{\sqrt{K}}{V} \zeta_\phi \end{aligned} \quad (\text{Equation 5})$$

where ζ_V and ζ_ϕ are Gaussian white noises of variance unity. Here, γ^{-1} is the typical timescale of the actin flow fluctuations

parts. Assuming that, for any given experimental condition, the cell velocity is directly proportional to the actin flow velocity ($\mathbf{v} = \alpha \mathbf{V}$, where we set hereafter $\alpha = -1$ for the sake of simplicity), Equation 5 makes it possible to fully characterize the resulting cell trajectories. In particular, the steady-state distribution $P(v)$ of the velocity can be obtained as (see [Supplemental Information](#)):

$$P(v) = \frac{N}{\sigma^2(v)} \exp \left(2\gamma \int_0^v du \frac{\mathcal{F}(u)}{\sigma^2(u)} \right) \equiv N e^{-\gamma W(v)}, \quad (\text{Equation 6})$$

where $W(v)$ is an effective potential ([Figures 4C–4E](#)) and N a normalization constant, and the persistence time can be deduced from the analysis of the autocorrelation function. In turn, the polarization time τ_p (defined as the mean lifetime of a cellular configuration, [Figure 3C](#)) can be analytically obtained as the mean first-passage time ([Condamine et al., 2007](#)) at $v = 0$ (see [Supplemental Information](#)).

The analysis of the model reveals that the polarization time $\tau_p(v)$ (obtained analytically) and persistence time $\tau(v)$ (obtained from Monte Carlo simulations of Equation 5) can be very well

approximated by a simple exponential $\tau, \tau_p \approx Ae^{n\nu}$ in dimensions 1, 2, and 3 for a wide range of parameters as soon as the Hill index satisfies $0.7 < n < 1.5$, which shows that no strong nonlinearity needs to be invoked to fit the data. Remarkably, this allowed us to fit all the available data (Figures 4A and S4; Table S1) with a single universal exponential master curve and therefore reproduce quantitatively the UCSP law. This provides a first clear validation of the model.

Synthetic Engineering of a UCSP Module Using an Optogenetic Approach

The mechanism underlying our model is that the advection of a rear-associated polarity cue from the cell leading edge to the rear (of the cell or of a protrusion) by the actin retrograde flow would contribute to the concentration of the cue at the rear and depletion from the front. This would reinforce cell polarity (or increase the lifetime of the protrusion), thus increasing cell speed and persistence, generating a positive feedback loop. To prove it experimentally, we developed a synthetic system based on Arpin and on the CRY2/CIBN optogenetic tool (Figure 5A). Arpin is a negative regulator of the Arp2/3 complex that is known to decrease lamellipodial protrusion and that does not directly bind to actin (Dang et al., 2013). CRY2 and CIBN are two independent proteins that rapidly form a heterodimer after blue light illumination (Kennedy et al., 2010). To directly test the central hypothesis of our model, we fused Arpin to CRY2 (and to mCherry to track Arpin localization), while two actin binding proteins that strongly differ in their affinity to actin, LifeAct and Utrophin-CH (Utr) (Figure 2F), were fused to CIBN (and to GFP). As expected, these fused proteins localized constitutively to actin filaments. While blue light illumination did not modify cytoplasmic localization of Arpin-CRY2 expressed alone, when it was co-expressed with LifeAct-CIBN or Utr-CIBN, blue light illumination induced its recruitment to actin filaments (Figure 5B; Movie S4). To simplify the analysis, cells were plated on thin line patterns, thus imposing a single protrusion (Doyle et al., 2009) and only two possible directions of migration. Continuous whole cell blue light illumination generated concentration gradients of Arpin-CRY2 from front to back of the cell, reflecting the binding of Arpin-CRY2 to actin and its advection with the retrograde flow (Figure 5C). Upon binding through Utrophin-CIBN the concentration profile rapidly changed to reach a new steady state within ~ 10 min (Figure 5D). Different steady-state slopes were generated based on the association time of actin-binding proteins to actin, faint for LifeAct-CIBN, but much stronger for Utrophin-CIBN (Figure 5E), as expected from Figure 2F. This artificial system thus proved well suited to test our model: a negative regulator of actin polymerization, Arpin, was advected back from the cell leading edge by the actin retrograde flow, and the advection was more efficient for a stronger binding to actin.

We next assessed how this advection would affect cell migration. As expected, Arpin-CRY2 overexpression alone strongly impaired both cell speed and persistence (Dang et al., 2013), and co-expression of LifeAct-CIBN, which produces a weak backward advection of Arpin, was not able to rescue this effect after blue-light illumination. Conversely, co-expression of Utrophin-CIBN completely rescued cell speed and persistence time (Figures 5F and 5G), consistent with the different advection rates

of the Utrophin and Lifeact probes. To rule out that this effect was due to more efficient global depletion of Arpin from the cytoplasm upon binding to actin filaments via the Utrophin probe, we measured Arpin-CRY2 depletion from the cytoplasm after light-induced recruitment to the actin cytoskeleton via LifeAct-CIBN or Utrophin-CIBN. This showed that depletion was similar for both probes (Figure 5H). We could thus conclude that the rescue of cell speed and persistence observed with the Utrophin probe was specifically due to the advection of Arpin by the actin retrograde flow. This set of experiments provided two important validations of our model: first it showed that the effect of actin retrograde flow on cell persistence, via stabilization of a protrusion, which we observed in dendritic cells, could be reproduced in a completely different cell type, RPE1 cells. Second, it showed that direct engineering of an artificial system involving the minimal set of elements used in our model was enough to recapitulate the effects predicted by the model.

Phase Diagram of Main Cell Migration Patterns

In addition to the prediction of the UCSP, our model provides through Equation 5 an explicit construction of a cell trajectory as that of an active Brownian particle (Romanczuk et al., 2012). While this concept has already proved to be useful to model phenomenologically cell trajectories (Selmeczi et al., 2008), so far no such bottom up approach was available. The analysis of Equation 5 yields a very rich phase diagram as a function of β and C_s , which predicts three main classes of trajectories, as detailed below (Figures 4B–4H and S5; see Supplemental Information for details).

Brownian Trajectories

For β smaller than a critical value $\beta_c(C_s)$, the potential $W(v)$ has a generic bowl shape centered at $v = 0$ and the process can be well approximated by a classical Ornstein Uhlenbeck process (Gardiner, 2004) (Figures 4B, 4C, and 4F). This regime of slow maximal actin flow is characterized by an autocorrelation of v that decays exponentially with a short characteristic time $\tau \sim 1/\gamma$, so that there is no stable polarized state. At time scales larger than $1/\gamma$ trajectories are then Brownian like.

Persistent Trajectories

For $\beta > \beta_c(C_s)$ and C_s larger than a critical value $C_s^c(\beta)$, $W(v)$ has a “sombbrero shape,” which is the hallmark of systems with broken symmetry (Figures 4B, 4D, and 4G). In this regime of fast maximal actin flow and large maximal concentration of activated cues, the modulus of the velocity v fluctuates around a non-zero average. Trajectories then correspond to a persistent random walk with long lived polarization time, which is exponentially larger than $1/\gamma$.

Intermittent Trajectories

For $\beta > \beta_c(C_s)$ and $C_s < C_s^c(\beta)$, $W(v)$ as a mixed shape, with both a local minimum around $v = 0$ and a secondary minimum for a non-zero value of v (Figures 4B, 4E, and 4H). This regime of fast maximal actin flow and small maximal concentration of activated cues leads to intermittent trajectories (Bénichou et al., 2011), characterized by an alternation of Brownian and persistent phases. The stabilization of the Brownian phase (around $v = 0$) is due to the multiplicative noise term in Equation 5 (see Mallick and Marcq, 2004): the small maximal concentration of activated cues induces large fluctuations that are enhanced for large actin

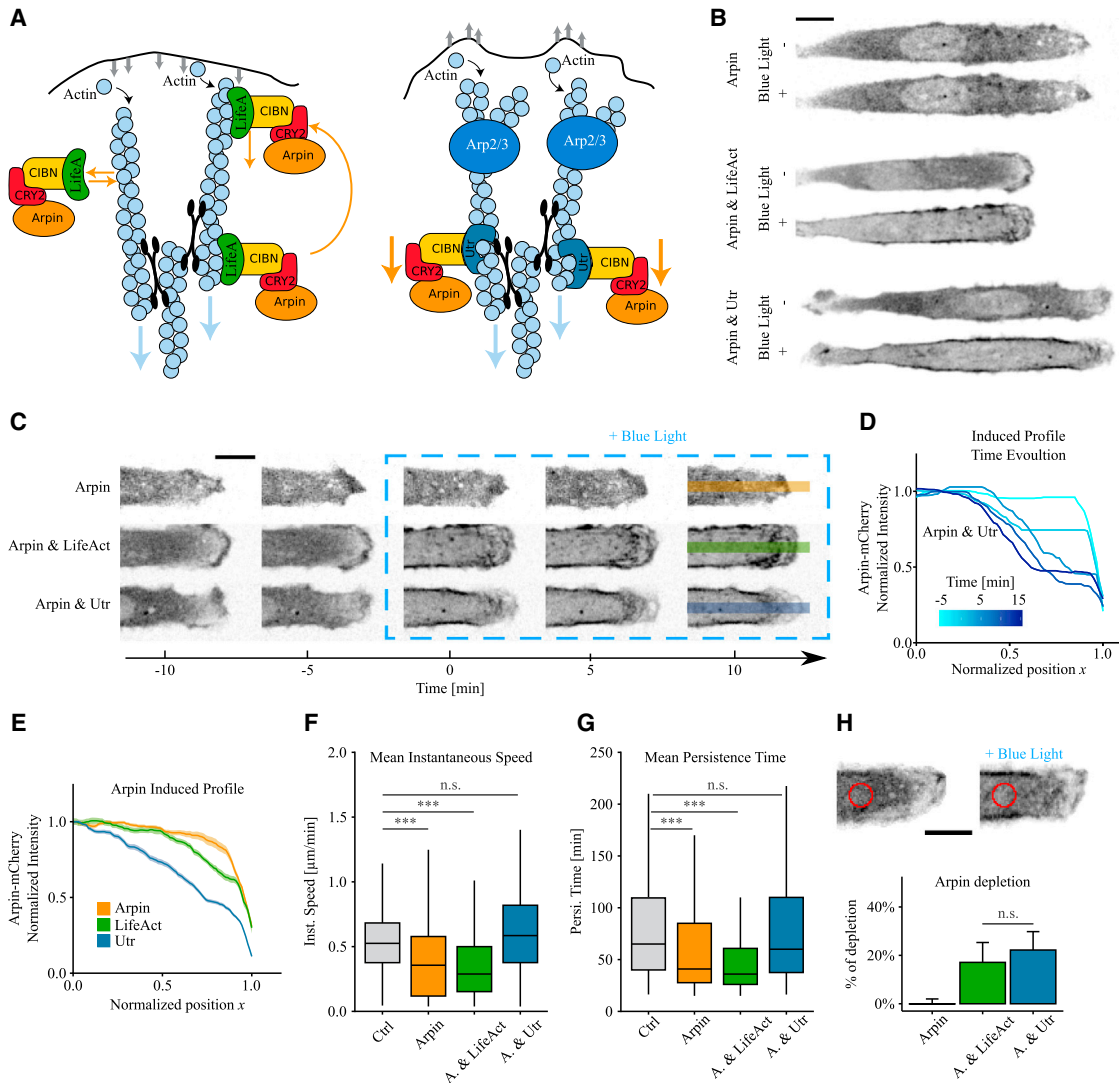


Figure 5. Optically Triggered Advection of Arpin by the Actin Retrograde Flow

(A) Schematic of the principle of the experiment: Arpin-CRY2 overexpression inhibits Arp2/3-dependent actin polymerization. Blue light illumination induces CIBN/CRY2 heterodimerization and the subsequent transient binding of Arpin-CRY2 to the co-expressed actin binding protein, LifeAct-CIBN (left) or Utr-CIBN (right). Binding to Utr-CIBN, but not binding to LifeAct-CIBN, induces depletion of Arpin from the leading edge. (B–H) RPE1 cells plated on 9- μm wide fibronectin-coated line micro-patterns, transiently transfected with three sets of constructs: Arpin-CRY2-mCherry alone, Arpin-CRY2-mCherry and LifeAct-CIBN(-GFP), or Arpin-CRY2-mCherry and Utr-CIBN(-GFP). (B) Confocal images of Arpin-CRY2-mCherry before (–) and after (+) blue light illumination in representative cells expressing the three sets of constructs. (C and D) Time-lapse images of the leading edge of the cells shown in (B). (D) Time evolution of Arpin-CRY2-mCherry fluorescence intensity profile after light-induced binding to Utr-CIBN in the leading edge of a representative cell. Time is color-coded. In (D) and (E), the normalized position x is defined along the cell polarity axis, where the cell front is set at $x = 1.0$. (E) Average steady state and SE of normalized Arpin-CRY2-mCherry fluorescence intensity profiles after blue light illumination at the leading edge of moving cells transfected with the three sets of constructs. (F and G) Instantaneous speed (F) and persistence time (G) of non-transfected cells (Ctrl) or cells transfected with the three sets of constructs. In boxplots: middle bars are medians, the rectangles span from the first to the third quartiles and bars extent from $\pm 1.5 \times \text{IQR}$. One-tailed t test. (H) Arpin-CRY2-mCherry depletion from the cytoplasm. Fluorescence was measured in the cytoplasm away from actin rich regions (red circle, top panel) for cells expressing the three sets of constructs (two-tailed t test, error bars are SD). *** $p < 0.001$, n.s. not significant. See also [Movie S4](#).

flows. The resulting dependence on v of the noise intensity leads to an effective restoring force toward the unpolarized state $v = 0$.

The analysis above shows in particular that the general coupling that we describe between actin flow and polarity cues is in principle sufficient to induce cell polarization (see the transi-

tion from diffusive to persistent or intermittent trajectories for increasing β). We, however, do not claim that this is the only mechanism responsible for cell polarization. In fact, a preexisting polarization mechanism, for example of Turing type, can be included in the model (see [Supplemental Information](#)). In such

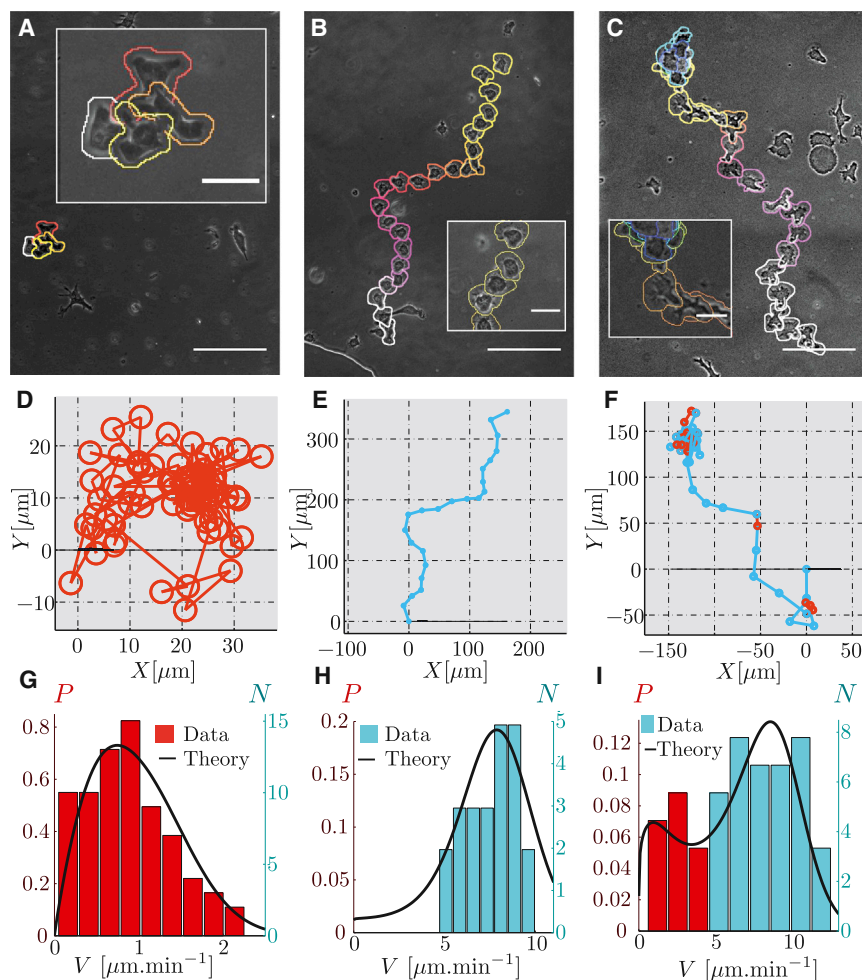


Figure 6. Experimental Cell Trajectories Can Be Classified in the Three Classes Predicted by the Model

Experimental cell trajectories can be classified in the three classes predicted by the model: diffusive (A, D, and G), persistent (B, E, and H), and intermittent (C, F, and I).

(A–C) Examples of BMDCs migration patterns of each type (temporal overlay of phase contrast images). Color code indicates the time course (total duration: (A) 276 min, (B) 72 min, and (C) 141 min. Scale bar, 100 μm (insets: 25 μm).

(D–F) Corresponding trajectories extracted from automated tracking of the nucleus. Circles indicate the confidence interval (3 μm). Blue stands for cell speed $v > 4 \mu\text{m}\cdot\text{min}^{-1}$ and red for $v < 4 \mu\text{m}\cdot\text{min}^{-1}$.

(G–I) Histograms of velocities extracted from the corresponding experimental tracks are in agreement with the distribution of velocities $P(v)$ (solid black line) from the model with parameters determined in the Supplemental Information and β, C_s as indicated in Figure 4B: diffusive phase (+), persistent (*), and intermittent (x). See also Movie S5.

a case, we found that the coupling to actin flows again results in an increased polarization lifetime and thus an increase in cell persistence. This shows the validity of the UCSP independently of the presence of a preexisting polarization mechanism.

The three classes of trajectories predicted by the model have been reported repeatedly in the literature (Selmecki et al., 2008; Vedel et al., 2013), which provides a further validation of the model. To test this prediction more quantitatively, we analyzed 2D trajectories of BMDCs (Figures 6A–6F; Movie S5) obtained by automated tracking of cell nuclei. For each analyzed trajectory, the measured velocity distribution $P(v)$ could be well fitted by the model by adjusting only β and C_s , while all other parameters values were kept as in Figure 4 (Figures 6G–6I). We found that indeed all trajectories could be classified according to the above 3 classes predicted by the model (Brownian, persistent, intermittent) depending on the value of the parameters β and C_s only, in agreement with the predicted phase diagram (Figure 4B).

DISCUSSION

Maintenance of cell polarity in time determines long-term cell migration patterns. Different molecular regulators of cell polarity

in motile cells have been identified in the past. However, mechanistic models with predictive capacity from molecular scales to global cell behavior (e.g., cell shape, speed, and persistence) remain sparse mainly due to a limitation of experimentally accessible parameters and the large number of involved components. In this work, we describe a positive feedback loop between actin flows and maintenance of cell polarity in motile cells.

This positive feedback impacts on the long-term migration behavior of cells and results in a higher persistence for faster cells—the UCSP law. By combining experimental results with theoretical modeling we suggest that actin flows are involved in reinforcing an asymmetric molecular distribution during cell polarization and thus increasing polarization lifetime. The two main predictions of the model were validated experimentally: (1) we first showed that it quantitatively predicts the UCSP law, and (2) we next demonstrated that it reproduces the main migratory behaviors reported so far. In addition, we could engineer a synthetic module based on the main ingredients of the model, to optically modulate the UCSP. We thus believe that our model provides an important step toward a comprehensive view on cell motility from microscopic to large-scale cell behavior.

The persistence time depends exponentially on the mean instantaneous velocity—that characterizes the UCSP—(Figure 1) in the lower range of speeds for each cell type, and a saturation to a plateau is observed at larger speeds. Such saturation could have several causes. The model primarily predicts an exponential dependence of the polarization time τ_p on the actin flow speed V . Such dependence $\tau_p(V)$ implies a similar exponential dependence $\tau(v)$ between persistence time and cell speed

under two conditions. First, it requires that polarization time τ_p and persistence time τ can be identified. While this is clear in 1D geometries, this does not always hold in dimensions 2 and 3, where two effects compete to destroy persistence: depolarization, characterized by the timescale τ_p , and angular diffusion, characterized by the timescale $\tau_\phi \sim \beta^2/K$. One therefore expects that $\tau \sim \tau_p$ only for $\tau_p \leq \tau_\phi$, while τ saturates for larger values of τ_p . Second, it requires that cell speed and actin flow speed are linearly coupled ($v = \alpha V$). As we argued, such linear dependence generally holds in the lower range of speeds for each cell type. Non-linear effects (that could be due for example to a motor-clutch mechanism) (Mitchison and Kirschner, 1988) are, however, expected at larger speeds and could result in the observed saturation of the persistence time.

An important observation we made is that this law also applies at the subcellular scale, to individual cell protrusions. This has two consequences: first it explains why cells with various modes of migration follow the UCSP law, as it might apply to any locomotory subpart of the cell and the nature of the protrusions does not matter. Second, it suggests that such coupling between actin filaments flow rate (or even flows of other cytoskeletal elements) and lifetime of polarity might apply to other phenomena than cell migration, such as polarized secretion or growth, which also rely on actin polymerization.

In this work, we have validated the law on cells of mammalian origin migrating in 1D and 2D geometries, with or without confinement and in 3D collagen gels—the main *in vitro* migration assays. We also extended our finding to myeloid cells moving in live tissues in Medaka fish. The process we describe is so generic, that it is likely to apply to cells from other organisms. Indeed a very similar correlation between speed and persistence was reported from migrating amoeba (Miyoshi et al., 2003; Golé et al., 2011). This law a priori only applies to random migration and not to guided migration. It is, however, likely that the mechanism that we describe helps reinforce a weak external guidance and it might thus be also important for guided migration. As a first modeling step in that direction, we showed that our model and the UCSP still hold if an independent polarization module exists.

In this work, we did not aim at investigating in more details the molecules that might, for a given cell type, be responsible for coupling the flow to the polarity. We believe that, even in a given cell type, there might be several molecules that could contribute to the coupling. For example, one of the most obvious player would be Myosin II, as it fits the two requirements: it is transported by actin filaments and the steepest its gradient, the faster the flow. Such a mechanism inspired us in the choice of the feedback equation we used in the model (Equation 3). This hypothesis was validated in the case of BMDCs, which are typical amoeboid cells whose motility strongly relies on the activity of Myosin II. Nevertheless, inhibiting Myosin II was also shown to induce a stronger Rac-dependent protrusive activity and thus a stronger polymerization-based actin flow (Sanz-Moreno et al., 2008), which can also transport polarity cues and thus compensate for the loss of Myosin II, at least in protrusion-based migration in mesenchymal cells. Last, we stress that our analysis does not exclude polarity cues involved in the regulation of other key actors of cell polarity such as microtubules (Zhang et al., 2014), as long as they interact at least indirectly with actin.

One of the most promising aspect of the model we have proposed based on the UCSP, is that it can generate all the range of observed cell trajectories, with only two main parameters: the maximal actin flow velocity β and the maximal concentration of activated cues C_s . While the latter might be difficult to vary experimentally, we have shown that the former is in fact quite versatile (Figure 2A), which opens the way to the control of cell migration patterns. We could experimentally implement an optogenetic synthetic module that performs that task by inducing binding of a negative regulator of actin polymerization (Arpin) to actin filaments. Upon blue light illumination, Arpin was coupled to Utrrophin and thus depleted from the migration front by retrograde advection with the actin flow, which in turn stabilized the protrusion. It is possible that some cells regulate binding of polarity factors to actin to tune their persistence. Making use of recent results that identified optimal search patterns for both persistent (Tejedor et al., 2012) and intermittent trajectories (Bénichou et al., 2011), we anticipate that the search efficiency for a target (e.g., DCs searching for antigens in a tissue) (Heuzé et al., 2013) could be optimized by tuning β and C_s . The model we propose thus provides a very generic ingredient of cell migration that could be used as a basis to model any process in which individual cell trajectories matter, such as search processes by immune cells (Harris et al., 2012), neuronal cells migration, or invasion by cancer cells.

EXPERIMENTAL PROCEDURES

In brief (see the [Extended Experimental Procedures](#) for a detailed description of the methods), bone marrow-derived dendritic cells were generated from the bone marrow extracted from mice and cultured as previously described. Human retinal pigment epithelial (RPE1, Clontech) were grown in standard conditions. Medaka fish: (*Oryzias latipes*) stocks were maintained as previously described. *Itgb2^{-/-}*, *Itgb2^{-/-} LifactGFP*, and wild-type mice were kept on a C57BL/6 background and bred in a conventional animal facility at IST Austria according to local regulations.

For 1D migration assays, RPE1 cells were placed on line-shaped micro-patterns coated with fibronectin, and BMDCs into fibronectin-coated microchannels. For 2D migration, cells were either regularly plated on a fibronectin-coated surface, or plated between two surfaces separated by micro-fabricated spacers to introduce confinement. To obtain large cell tracking area, nine adjacent fields of views were recorded and images stacks were stitched by a custom written software. For 3D migration, collagen gels were prepared using 1.6 mg/ml of bovine collagen (PureCol, Advanced BioMatrix). BMDCs were embedded in polymerizing collagen and then immediately confined between two glass surfaces spaced 5 μm apart.

Medaka myeloid cells live imaging was performed on fish at 9–11 days post-fertilization mounted as previously reported. Under-agarose-assays were performed with cells inserted between an agar gel and a Petri dish, as previously described. Blebbistatin (Sigma) was used in a final concentration of 10–20 μM . ML-141 (Sigma) was used at a final concentration of 20 μM . BMDCs and RPE1 cells were transfected using commercial transfection kit (from Amaxa and Roche or Invitrogen, respectively) according to the manufacturers recommendations. Nuclei were stained with Hoechst.

Time-lapse movies of cell nuclei in 1D, 2D, 3D, and *in vivo*, were analyzed by a custom written program as previously described. Medaka myeloid cells and BMDCs under-agarose were manually tracked with Fiji. In 1D, the persistent time is defined as the time a cell moves in the same direction, in 2D, 3D, and *in vivo*, as the time it takes for the cell to change its initial direction by 90°. The differential angle is the angle between two consecutive displacements of a cell. BMDCs under-agarose tracks were analyzed using in-house algorithms implemented in MATLAB (MathWorks). The mean-square displacement (MSD) was fitted according to the Furths formula in order to extract the

persistence time. Actin dynamics were analyzed by kymographs as previously described. Protein relocalization was quantified using Fiji. For the analysis of polarization lifetimes migrating cells were imaged every 10 s and the number of protrusions were recorded and saved as vectors.

RPE1 cells transfected with Arpin-CRY2-mCherry were imaged with an inverted spinning disk confocal microscope (Roper/Nikon) with 60× magnification. mCherry channel was acquired every minute, then after 10 min, Arpin-CRY2-mCherry recruitment to F-actin (using actin-bound LifeAct-CIBN-GFP or Utrophin-CIBN-GFP) was induced by illuminating also in the GFP channel. For statistical analysis of trajectories, cells were imaged at lower magnification (5×) with illumination in the GFP channel at each time point (time-lapse 5 min).

Medaka fish (kindly provided by J. Wittbrodt) were kept and treated in accordance with the German (Tierschutzgesetz) or Italian (decree 116/92) national guidelines and experimental procedures were approved by Institutional Animal Care and Use Committee. Mice were bred in conventional animal facilities at IST Austria or at the Institut Curie according to local regulations.

SUPPLEMENTAL INFORMATION

Supplemental Information includes Supplemental Experimental Procedures, Supplemental Discussion, five movies, five figures, and one table and can be found with this article online at <http://dx.doi.org/10.1016/j.cell.2015.01.056>.

AUTHOR CONTRIBUTIONS

P.M. was in charge of the project and performed the cell trajectory analysis. J.F.R. was the main contributor for the modeling and performed the simulations. S.W. performed and analyzed the experiments on dendritic cells presented in Figures 2 and 3. O.B. and N.G. contributed to the modeling. V.R. contributed to the experiments and analysis on dendritic cells presented in Figures 2 and 3. P.M., N.C., M.C., and S.D.B. designed the optogenetic tools and preformed experiments of Figure 5. F.L., M.L.B., M.R., and H.R.T. performed cell migration experiments presented in Figures 1 and 6. C.L.C. performed the experiments on myeloid cells in live Medaka fish presented in Figure 1. C.P.H. supervised the work of V.R. A.-M.L.-D. supervised the experiments on dendritic cells presented in Figure 1. M.S. supervised the work of S.W. and contributed to the writing of the article. R.V. supervised the modeling, the work of J.F.R., and wrote the article. M.P. coordinated the study, supervised the work of P.M., F.L., M.L.B., M.R., and H.R.T., and wrote the article.

ACKNOWLEDGMENTS

We acknowledge J. Wittbrodt for providing the medaka fish transgenic line and D. Riveline and J.F. Joanny for discussions and comments on the manuscript. The authors greatly acknowledge Lucie Sengmanivong from the Nikon Imaging Centre at Institut Curie-CNRS and Vincent Fraisier from the PICT-IBISA Lhomond Imaging facility of Institut Curie for their help on microscopy. P.M. was supported by a “Fondation pour la Recherche Medicale” fellowship. V.R. was supported by the Austrian Science Fund (FWF) T560-B17. C.L.C. was supported by grant AIRC-IG and PRIN 2010-2011 to Ruggero Pardi. F.L. was supported by EMBO ALTF 1163-2010. O.B., R.V., and M.P. were supported by ANR (ANR-09-PIRI-0027) and InNaBioSant. M.P. was supported by ERC (311205-PROMICO). M.S. was supported by ERC (281556_Leukocyte Forces) and a HFSP Program Grant.

Received: February 4, 2014
Revised: November 25, 2014
Accepted: January 22, 2015
Published: March 19, 2015

REFERENCES

Bénichou, O., Loverdo, C., Moreau, M., and Voituriez, R. (2011). Intermittent search strategies. *Rev. Mod. Phys.* 83, 81–129.

Bois, J.S., Jülicher, F., and Grill, S.W. (2011). Pattern formation in active fluids. *Phys. Rev. Lett.* 106, 028103.

Burkel, B.M., von Dassow, G., and Bement, W.M. (2007). Versatile fluorescent probes for actin filaments based on the actin-binding domain of utrophin. *Cell Motil. Cytoskeleton* 64, 822–832.

Callan-Jones, A.C., and Voituriez, R. (2013). Active gel model of amoeboid cell motility. *New J. Phys.* 15, 025022.

Condamin, S., Bénichou, O., Tejedor, V., Voituriez, R., and Klafter, J. (2007). First-passage times in complex scale-invariant media. *Nature* 450, 77–80.

Czirók, A., Schlett, K., Madarász, E., and Vicsek, T. (1998). Exponential distribution of locomotion activity in cell cultures. *Phys. Rev. Lett.* 81, 3038–3041.

Dang, I., Gorelik, R., Sousa-Blin, C., Derivery, E., Guérin, C., Linkner, J., Nemethova, M., Dumortier, J.G., Giger, F.A., Chipysheva, T.A., et al. (2013). Inhibitory signalling to the Arp2/3 complex steers cell migration. *Nature* 503, 281–284.

Doyle, A.D., Wang, F.W., Matsumoto, K., and Yamada, K.M. (2009). One-dimensional topography underlies three-dimensional fibrillar cell migration. *J. Cell Biol.* 184, 481–490.

Gardel, M.L., Schneider, I.C., Aratyn-Schaus, Y., and Waterman, C.M. (2010). Mechanical integration of actin and adhesion dynamics in cell migration. *Annu. Rev. Cell Dev. Biol.* 26, 315–333.

Gardiner, C. (2004). *Handbook of Stochastic Methods for Physics, Chemistry and Natural Sciences* (Berlin: Springer).

Goehring, N.W., Trong, P.K., Bois, J.S., Chowdhury, D., Nicola, E.M., Hyman, A.A., and Grill, S.W. (2011). Polarization of PAR proteins by advective triggering of a pattern-forming system. *Science* 334, 1137–1141.

Golé, L., Rivière, C., Hayakawa, Y., and Rieu, J.-P. (2011). A quorum-sensing factor in vegetative Dictyostelium discoideum cells revealed by quantitative migration analysis. *PLoS ONE* 6, e26901.

Grabher, C., Cliffe, A., Miura, K., Hayflick, J., Pepperkok, R., Rørth, P., and Wittbrodt, J. (2007). Birth and life of tissue macrophages and their migration in embryogenesis and inflammation in medaka. *J. Leukoc. Biol.* 81, 263–271.

Harris, T.H., Banigan, E.J., Christian, D.A., Konradt, C., Tait Wojno, E.D., Norose, K., Wilson, E.H., John, B., Weninger, W., Luster, A.D., et al. (2012). Generalized Lévy walks and the role of chemokines in migration of effector CD8+ T cells. *Nature* 486, 545–548.

Hawkins, R.J., Poincloux, R., Bénichou, O., Piel, M., Chavrier, P., and Voituriez, R. (2011). Spontaneous contractility-mediated cortical flow generates cell migration in three-dimensional environments. *Biophys. J.* 101, 1041–1045.

Heasman, S.J., and Ridley, A.J. (2008). Mammalian Rho GTPases: new insights into their functions from in vivo studies. *Nat. Rev. Mol. Cell Biol.* 9, 690–701.

Heuzé, M.L., Vargas, P., Chabaud, M., Le Berre, M., Liu, Y.-J., Collin, O., Solanes, P., Voituriez, R., Piel, M., and Lennon-Duménil, A.-M. (2013). Migration of dendritic cells: physical principles, molecular mechanisms, and functional implications. *Immunol. Rev.* 256, 240–254.

Hong, L., Kenney, S.R., Phillips, G.K., Simpson, D., Schroeder, C.E., Nöth, J., Romero, E., Swanson, S., Waller, A., Strouse, J.J., et al. (2013). Characterization of a Cdc42 protein inhibitor and its use as a molecular probe. *J. Biol. Chem.* 288, 8531–8543.

Jülicher, F., Kruse, K., Prost, J., and Joanny, J.F. (2007). Active behavior of the cytoskeleton. *Phys. Rep.* 449, 3–28.

Jurado, C., Haserick, J.R., and Lee, J. (2005). Slipping or gripping? Fluorescent speckle microscopy in fish keratocytes reveals two different mechanisms for generating a retrograde flow of actin. *Mol. Biol. Cell* 16, 507–518.

Kennedy, M.J., Hughes, R.M., Peteya, L.A., Schwartz, J.W., Ehlers, M.D., and Tucker, C.L. (2010). Rapid blue-light-mediated induction of protein interactions in living cells. *Nat. Methods* 7, 973–975.

Kondo, T., Hamao, K., Kamijo, K., Kimura, H., Morita, M., Takahashi, M., and Hosoya, H. (2011). Enhancement of myosin II/actin turnover at the contractile ring induces slower furrowing in dividing HeLa cells. *Biochem. J.* 435, 569–576.

- Lämmermann, T., Renkawitz, J., Wu, X., Hirsch, K., Brakebusch, C., and Sixt, M. (2009). Cdc42-dependent leading edge coordination is essential for interstitial dendritic cell migration. *Blood* *113*, 5703–5710.
- Maiuri, P., Terriac, E., Paul-Gilloteaux, P., Vignaud, T., McNally, K., Onuffer, J., Thorn, K., Nguyen, P.A., Georgoulia, N., Soong, D., et al. (2012). The first world cell race. *Curr. Biol.* *22*, R673–R675.
- Mallick, K., and Marcq, P. (2004). Noise-induced reentrant transition of the stochastic Duffing oscillator. *Eur. Phys. J B* *38*, 99–102.
- Mitchison, T., and Kirschner, M. (1988). Cytoskeletal dynamics and nerve growth. *Neuron* *1*, 761–772.
- Miyoshi, H., Masaki, N., and Tsuchiya, Y. (2003). Characteristics of trajectory in the migration of *Amoeba proteus*. *Protoplasma* *222*, 175–181.
- Mogilner, A., and Oster, G. (1996). Cell motility driven by actin polymerization. *Biophys. J.* *71*, 3030–3045.
- Munro, E., Nance, J., and Priess, J.R. (2004). Cortical flows powered by asymmetrical contraction transport PAR proteins to establish and maintain anterior-posterior polarity in the early *C. elegans* embryo. *Dev. Cell* *7*, 413–424.
- Ofer, N., Mogilner, A., and Keren, K. (2011). Actin disassembly clock determines shape and speed of lamellipodial fragments. *Proc. Natl. Acad. Sci. USA* *108*, 20394–20399.
- Poincloux, R., Collin, O., Lizárraga, F., Romao, M., Debray, M., Piel, M., and Chavrier, P. (2011). Contractility of the cell rear drives invasion of breast tumor cells in 3D Matrigel. *Proc. Natl. Acad. Sci. USA* *108*, 1943–1948.
- Renkawitz, J., Schumann, K., Weber, M., Lämmermann, T., Pflicke, H., Piel, M., Polleux, J., Spatz, J.P., and Sixt, M. (2009). Adaptive force transmission in amoeboid cell migration. *Nat. Cell Biol.* *11*, 1438–1443.
- Riedl, J., Crevenna, A.H., Kessenbrock, K., Yu, J.H., Neukirchen, D., Bista, M., Bradke, F., Jenne, D., Holak, T.A., Werb, Z., et al. (2008). Lifeact: a versatile marker to visualize F-actin. *Nat. Methods* *5*, 605–607.
- Romanczuk, P., Bar, M., Ebeling, W., Lindner, B., and Schimansky-Geier, L. (2012). Active Brownian particles from individual to collective stochastic dynamics. *Eur. Phys. J. Special Topics* *202*, 1–162.
- Sanz-Moreno, V., Gadea, G., Ahn, J., Paterson, H., Marra, P., Pinner, S., Sahai, E., and Marshall, C.J. (2008). Rac activation and inactivation control plasticity of tumor cell movement. *Cell* *135*, 510–523.
- Selmeczi, D., Li, L., Pedersen, L.I.I., Norrelykke, S.F., Hagedorn, P.H., Mosler, S., Larsen, N.B., Cox, E.C., and Flyvbjerg, H. (2008). Cell motility as random motion: a review. *Eur. Phys. J. Special Topics* *157*, 1–15.
- Svitkina, T.M., Verkhovskiy, A.B., McQuade, K.M., and Borisy, G.G. (1997). Analysis of the actin-myosin II system in fish epidermal keratocytes: mechanism of cell body translocation. *J. Cell Biol.* *139*, 397–415.
- Tejedor, V., Voituriez, R., and Bénichou, O. (2012). Optimizing persistent random searches. *Phys. Rev. Lett.* *108*, 088103.
- Theriot, J.A., and Mitchison, T.J. (1991). Actin microfilament dynamics in locomoting cells. *Nature* *352*, 126–131.
- Toner, J., Tu, Y., and Ramaswamy, S. (2005). Hydrodynamics and phases of flocks. *Ann. Phys.* *318*, 170–244.
- Vedel, S., Tay, S., Johnston, D.M., Bruus, H., and Quake, S.R. (2013). Migration of cells in a social context. *Proc. Natl. Acad. Sci. USA* *110*, 129–134.
- Vicente-Manzanares, M., Ma, X., Adelstein, R.S., and Horwitz, A.R. (2009). Non-muscle myosin II takes centre stage in cell adhesion and migration. *Nat. Rev. Mol. Cell Biol.* *10*, 778–790.
- Wilson, C.A., Tsuchida, M.A., Allen, G.M., Barnhart, E.L., Applegate, K.T., Yam, P.T., Ji, L., Keren, K., Danuser, G., and Theriot, J.A. (2010). Myosin II contributes to cell-scale actin network treadmill through network disassembly. *Nature* *465*, 373–377.
- Wu, P.-H., Giri, A., Sun, S.X., and Wirtz, D. (2014). Three-dimensional cell migration does not follow a random walk. *Proc. Natl. Acad. Sci. USA* *111*, 3949–3954.
- Zhang, J., Guo, W.-H., and Wang, Y.-L. (2014). Microtubules stabilize cell polarity by localizing rear signals. *Proc. Natl. Acad. Sci. USA* *111*, 16383–16388.

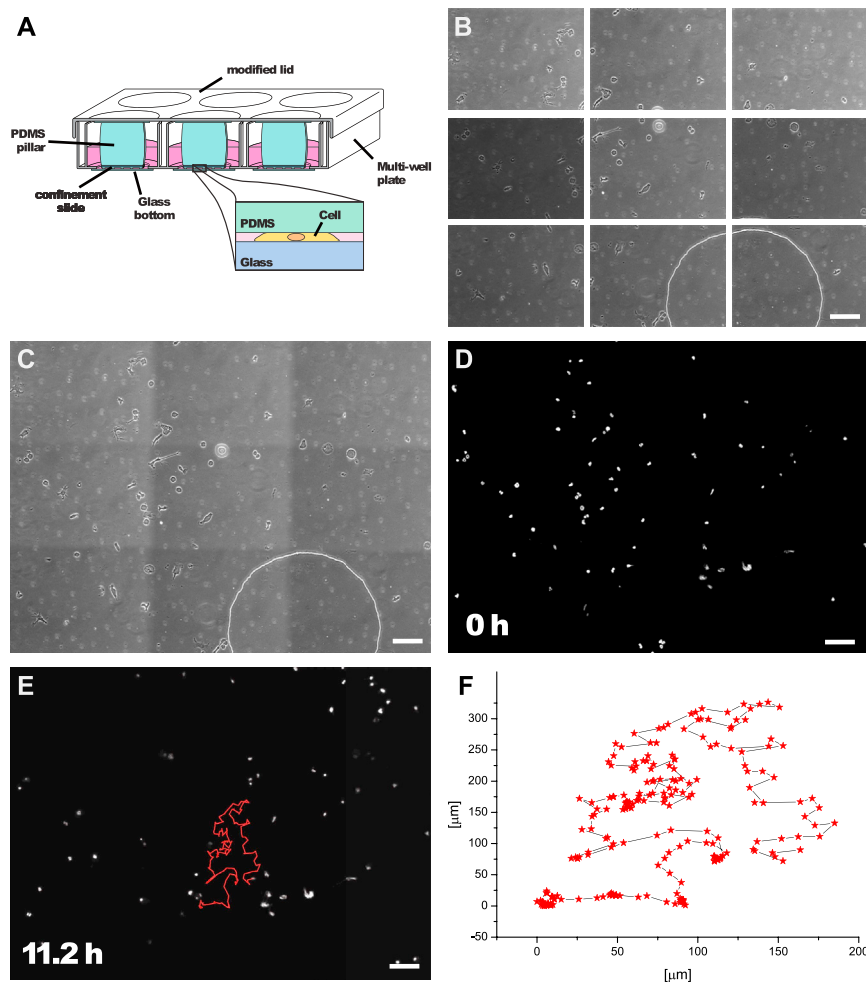
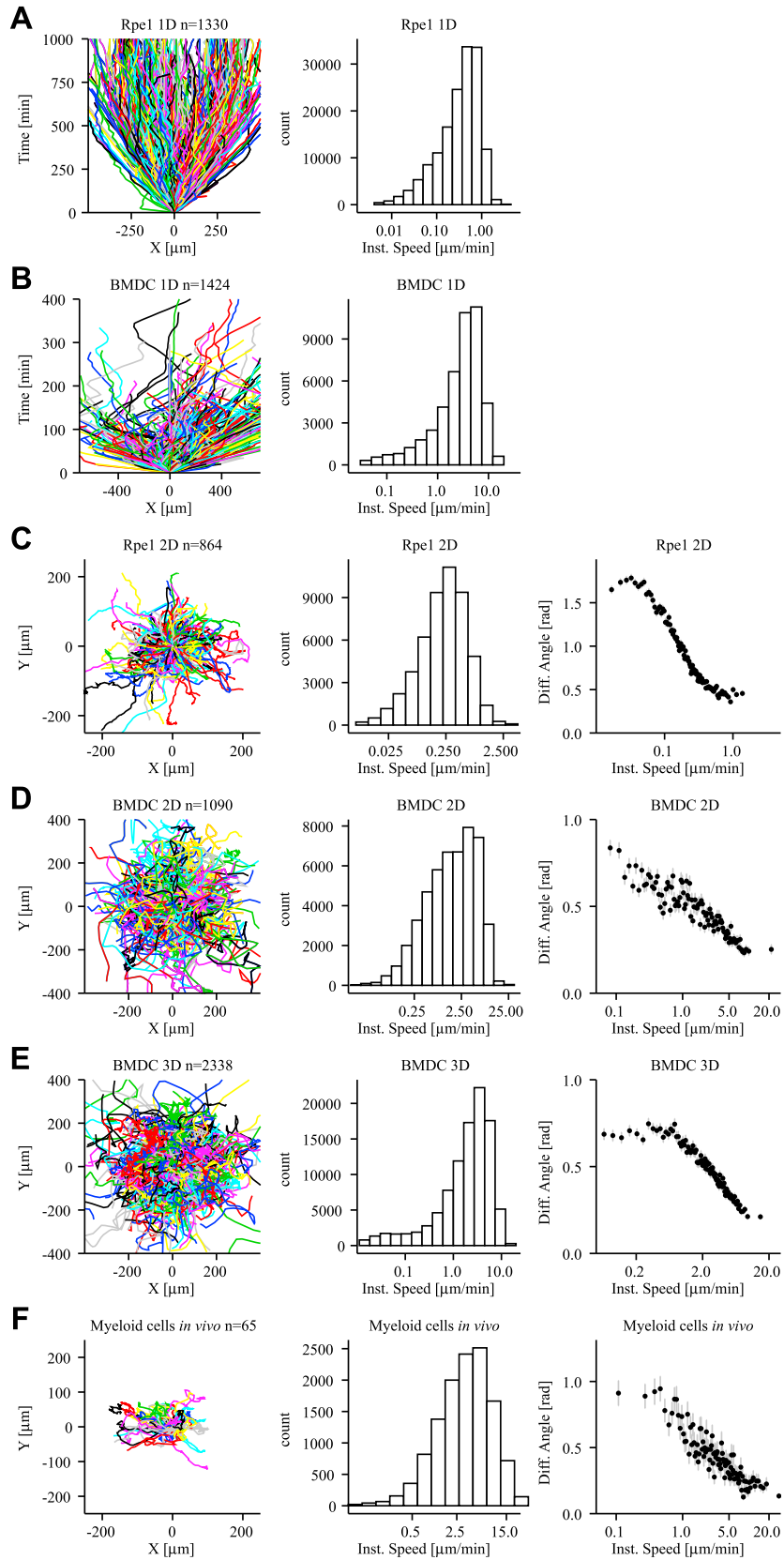


Figure S1. Set-Up for Stable 2D Time-Lapse Migration Assays over a Time Span >12 Hours, Related to Figure 1

- (A) Modified 6-well plate to confine cells. Modification consists of soft PDMS-pillar with additional confinement slide on the lid of the plate.
- (B) 9 individual, adjacent field of views were recorded every 3 min.
- (C) Individual fields were stitched to one single image.
- (D) Same procedure as in (B) and (C) was performed for nuclear Hoechst staining.
- (E and F) Individual nuclei were tracked with custom written software (E) and tracks used for further analysis (F). Scale bars in (B–E): 100 μm .



(legend on next page)

Figure S2. Cell Trajectories in 1D, 2D, 3D, and In Vivo, Related to Figure 1

(A and B) Rpe1 cells on 9 μm width fibronectin micropatterned lines and BMDC in fibronectin treated channels of $7 \times 5 \mu\text{m}^2$ section, respectively. Left: mono-dimensional single cell trajectories in time. Right: distribution of instantaneous speed.

(C–F) Rpe1 on 2D surface uniformly treated with fibronectin, BMDC confined between two planes 5 μm apart, BMDC embedded on bovine collagen gel and confined between two planes 5 μm apart and Medaka myeloid cells imaged in the fin of leaving fish, respectively. Left: single cell trajectories. Middle: distribution of instantaneous speed. Right: differential angle in function of instantaneous speed. Black dots and gray lines are mean and SE for the binned data.

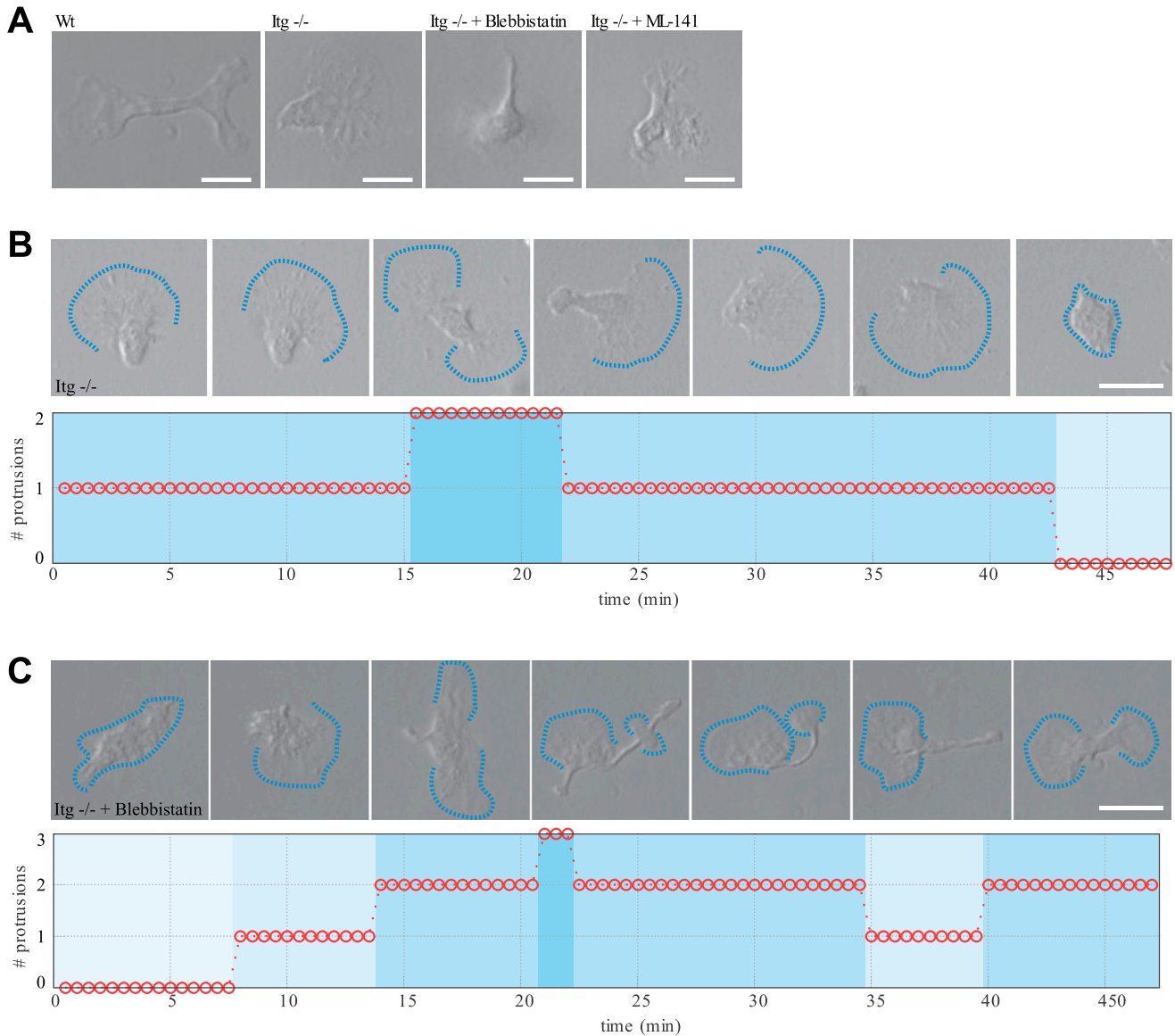


Figure S3. Stability of Cell Polarity in mBMDCs, Related to Figure 3

(A) Differential Interference Contrast (DIC) images showing representative examples for Wt mBMDCs, Itg^{-/-} mBMDCs, Itg^{-/-} mBMDCs treated with 20 μ M Blebbistatin and Itg^{-/-} mBMDCs treated with 20 μ M ML-141.

(B and C) Polarization lifetime analysis for (B) Itg^{-/-} dendritic cells and (C) Itg^{-/-} dendritic cells treated with 20 μ M Blebbistatin. During cell migration the number of protrusions were recorded over consecutive images and saved in vectors (state entries 0, 1, 2, 3 or higher). Two typical tracks with the number of protrusions as a function of time (bottom) are shown with according DIC images (top). All scale bars, 20 μ m.

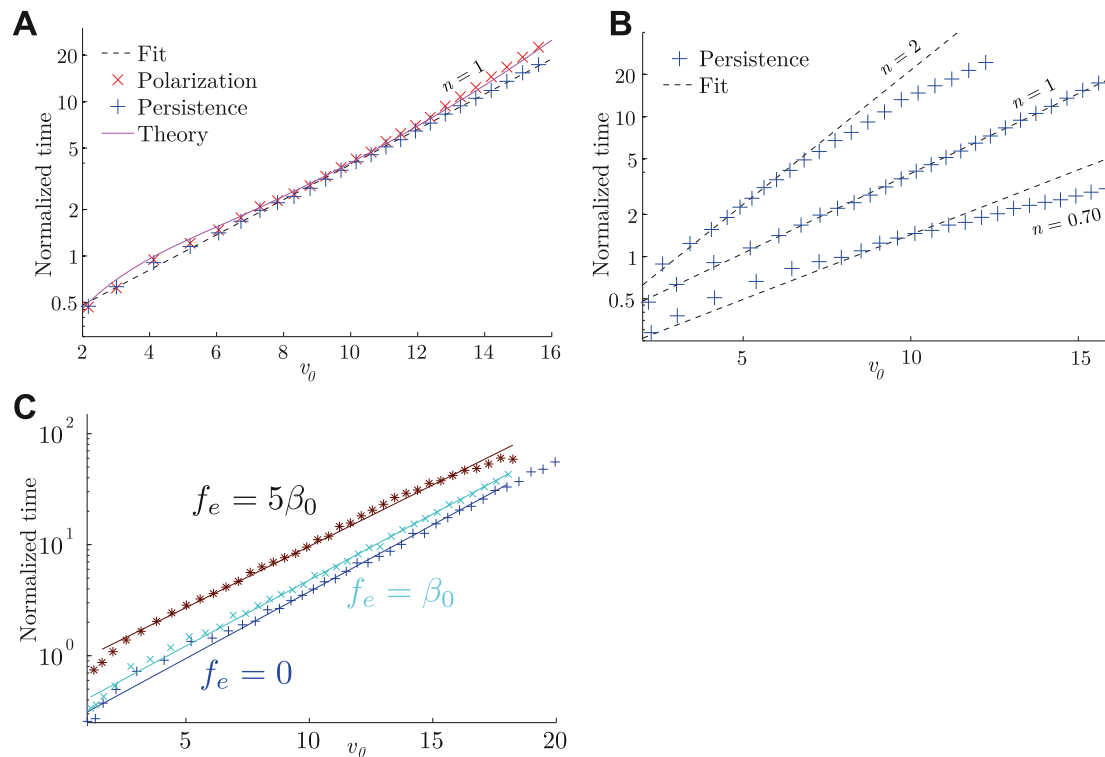


Figure S4. Theoretical Determination of Persistence and Polarization Times, Related to Figure 4

(A) The theoretical expression for the polarization function $T(V_f/V_0)$ (black solid line), i.e., the mean first passage time to reach $V_f = 0.10\beta_0$, is plotted as a function of an initial velocity $V_0 = \bar{V}$ equal to the mean velocity \bar{V} , and compared to both polarization (red x symbols) and persistence (blue + symbols) times determined from numerical simulations (case $n=1$). A linear fit is given in dashed line.

(B) Persistence time (obtained from numerical simulations) as function of the mean velocity for different hill exponents.

(C) Polarization time (from numerical simulations, symbols) for different strengths of a preexisting polarization mechanism. Linear fit given in solid line. The other parameters C_s , K and K_c are set in Sec. 2.6 for all panels.

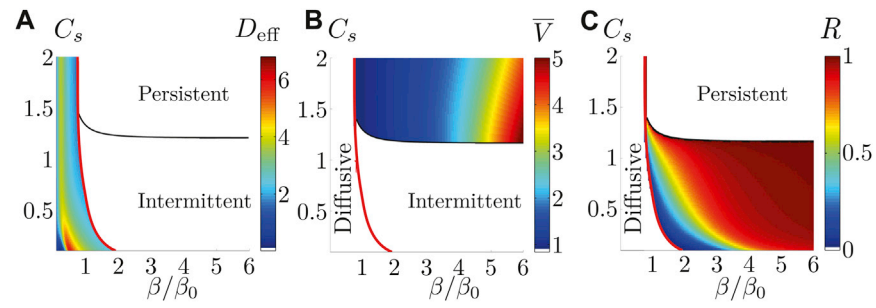


Figure S5. Phase Diagrams in Terms of the Coupling Strength β/β_0 and of the Saturation Level C_s , Related to Figure 4

(A) Effective diffusion coefficient D_{cell} of the cell within the diffusive phase.

(B) Mean velocity \bar{V} within the persistent phase.

(C) Ratio $R = \tau_1/(\tau_1 + \tau_2)$ of the time spent within the persistent phase τ_1 over the total time $\tau_1 + \tau_2$. The value of the parameter K_c is set in Sec. 2.6 and $K = 0$.